

PHI-MVS: Plane Hypothesis Inference Multi-view Stereo for Large-Scale Scene Reconstruction

Shang Sun, Yunan Zheng, Xuelei Shi, Zhenyu Xu, Yiguang Liu*

Abstract—PatchMatch based Multi-view Stereo (MVS) algorithms have achieved great success in large-scale scene reconstruction tasks. However, reconstruction of texture-less planes often fails as similarity measurement methods may become ineffective on these regions. Thus, a new plane hypothesis inference strategy is proposed to handle the above issue. The procedure consists of two steps: First, multiple plane hypotheses are generated using filtered initial depth maps on regions that are not successfully recovered; Second, depth hypotheses are selected using Markov Random Field (MRF). The strategy can significantly improve the completeness of reconstruction results with only acceptable computing time increasing. Besides, a new acceleration scheme similar to dilated convolution can speed up the depth map estimating process with only a slight influence on the reconstruction. We integrated the above ideas into a new MVS pipeline, Plane Hypothesis Inference Multi-view Stereo (PHI-MVS). The result of PHI-MVS is validated on ETH3D public benchmarks, and it demonstrates competing performance against the state-of-the-art.

Index Terms—Multi-view stereo, Markov Random Field, PatchMatch, large-scale, parallel computing.

I. INTRODUCTION

MULTI-VIEW STEREO(MVS) is an important research field in computer vision, and it aims to recover the three-dimensional structure of scenes using 2D images and camera parameters. The camera parameters (both internal and external parameters) can be obtained from the Structure From Motion software (such as Visual SFM[1], COLMAP[2]) or manual calibration. Nowadays, MVS can be used in many applications [3], [4], [5], [6] related to computer vision. Thanks to the public datasets and their online evaluation systems, it is becoming easier for authors to evaluate their algorithms. Depth-map merging based MVS aims to recover depth value for each pixel on every image and then merge them to obtain a final point cloud. The most popular way to implement stereo matching in the depth-map merging based MVS algorithm nowadays should be the PatchMatch[7].

However, when encountering texture-less regions, PatchMatch based method may become ineffective. There are two main reasons for the failure: First, to perform efficient stereo matching, local similarity measurement methods such as Normalized Cross Correlation(NCC) are widely used in the stereo matching step. As these methods can only reflect local similarity, there may exist plenty of wrong depth hypotheses whose similarity scores are even higher than that of ground truth on texture-less regions. Second, during the whole pipeline, random refinement is necessary to help the result jump out of local minimal. However, this procedure may also cause the result of texture-less regions to jump into

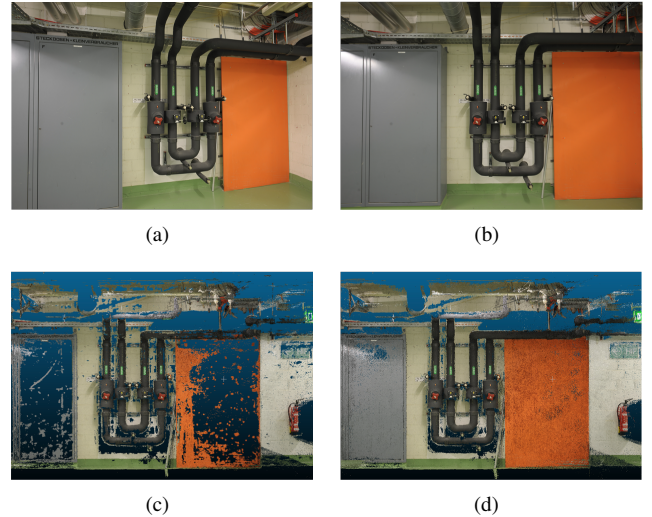


Fig. 1. (a) and (b) are input images of ETH3D dataset. (c) is the point cloud result without the plane hypothesis inference procedure, (d) is the result of our method.

wrong depth values whose similarity scores are higher than that of ground truth. Thus, we use an additional module to efficiently generate plane hypotheses with the filtered depth values output by stereo matching step, then choosing which hypothesis should be preserved by MRF. As the label number is small, the MAP inference of MRF can be executed within an acceptable time. Later, geometric consistency based filtering procedure is applied to remove outliers.

We know that the operation of accessing memory in the GPU unit consumes much time. Furthermore, by increasing support window size during stereo matching, the pixels' numbers will increase rapidly. To speed up our algorithm, we borrowed the idea from dilated convolution [8] during the stereo matching step. As shown in the experiment, our speed-up scheme is effective and can boost the algorithm with only a slight influence on the result.

Thus, we present PHI-MVS (Plane Hypothesis Inference Multi-View Stereo), a new MVS pipeline that has integrated our above ideas. The main contributions of PHI-MVS are as follows:

- A plane hypothesis generating and selecting strategy using MRF, which can improve the reconstruction on texture-less regions. The additional module can greatly increase the completeness of reconstruction with acceptable computing time consumption.
- A scheme similar to dilated convolution can speed up the

stereo matching step with only a slight influence on the accuracy and the completeness of results.

- A concise and practical MVS pipeline is proposed and the results on ETH3D high-resolution data set show its state-of-the-art performance.

II. RELATED WORK

MVS algorithms can be divided into four categories according to [9], they are voxel-based methods [10], [11], surface evolution-based methods [12], feature point growing-based methods [13], [14], and depth-map merging based methods [15], [16]. The proposed method belongs to the fourth category. Depth map-based MVS methods obtain a 3D dense model in two stages. First, the depth map is estimated for each reference image using stereo matching algorithms. Second, outliers are filtered, and a 3D dense model is obtained by merging all back-projected pixels.

In the early years, many algorithms [17], [18], [19], [20] use the Markov Random Field to solve stereo problems. These algorithms' main steps are as follows: First, they compute matching costs with discrete depth values or disparities for each pixel. Second, an energy equation that can be used to perform MAP inference is built. The energy function usually contains unary items and pairwise items. Unary items usually correspond to matching similarity, and pairwise items usually correspond to depth values' continuity and smoothness. Third, minimize the energy equation. As in general cases, minimize the energy equation is an NP-hard problem. Approximate minimization techniques such as [21], [22], [19] are usually used to solve the problem. The MRF-based methods have achieved satisfactory results as it is obvious that the depth values should be smooth and continuous between most neighboring pixels, except in the edge part. However, solving the energy function consumes a lot of memory and time. With the increase of image resolution and depth accuracy requirements, it is impossible to perform MRF-based methods within acceptable memory and time limits.

PatchMatch based algorithms gradually replaced the MRF-based algorithms in recent years. The first one that uses the PatchMatch algorithm to solve the stereo problem is [23]. Then [24] introduces this method to MVS problems. [25] is the first to implement the PatchMatch based algorithm on GPUs, and it uses the black-red pattern in the spatial spreading step. Nowadays, many algorithms [26], [27], [28] have achieved satisfactory performance. The main part of the whole pipeline is as follows: First, initializing the depth and normal values for each pixel using the random technique. Second, selecting neighboring images for each reference image. Third, performing stereo matching and spread good depth or normal hypothesis to neighboring pixels. Fourth, refining the depth and normal values with random disturb. Fifth, filtering the depth and normal vectors via geometric consistency. Last, back projecting pixels and merging them to a point cloud model. In each step, it may vary from one to another.

Deep learning has a significant influence on 3D vision. Recently, methods based on deep learning [29], [30], [31], [32], [33], [27] have achieved inspiring results. They can be

roughly divided into two categories. The first category is the end-to-end methods as [29], [32]. The main pipeline of these methods is as follows: First, use convolution networks to extract the original images' features. Transform pixels on the reference image to corresponding pixels on source images with discrete depth or disparity hypothesis. Compute the similarity of each depth hypothesis using the extracted features and obtain a cost volume. Second, different style neural networks are used to estimate the depth of the reference image based on the cost volume. Though they perform well on data sets [34], [35], many end-to-end methods could not work on ETH high-resolution benchmark according to [36]. Here are the reasons: Cost volume needs finite discrete depth values. With the increase of image resolution and depth accuracy requirements, these algorithms have to downsample the original images because of limited GPU memory. Besides, large viewpoint change breaks the assumption that neighboring images have a strong visibility association with the reference image. Though [36] try to handle the above issues, their performance on ETH3D still slightly lagging behind traditional methods. Other kinds of methods as [33], [27] use CNN as additional modules in the whole pipeline. Most of these methods aim to use CNN to predict the confidence of the depth and normal maps and then filter or pad the results using the confidence.

It is hard for PatchMatch based methods to recover correct depth information on texture-less regions. Many previous works [37], [33], [27], [33] have aimed to improve the reconstruction of these regions. However, most of these works either need segmentation information of original color images or based on data-driven deep learning methods. [37] handles this issue mainly by subdividing the image into superpixels. [27] estimates the confidence of the reconstructed depth map and then applies an interpolation stage. [33] uses the projection of points recovered by mesh and then uses CNN to filter outliers. [28] uses planar prior as guidance and geometric consistency during stereo matching.

III. PHI-MVS: THE METHOD

Our algorithm can mainly be divided into six parts: neighboring image selection, random initialization, depth map estimation, filtering, plane hypothesis inference, and fusion. We implement our method on GPUs with CUDA, and adopt the red-black pattern updating scheme in the spatial spreading step. To further speed up the algorithm, we adopt the improved red-black sampling method proposed by [38]. The goal of our whole pipeline is to estimate depth and normal values (d_x, n_x) for each pixels x on each reference image and then merge them to a single point cloud. The whole pipeline of the PHI-MVS is briefly shown in Algorithm 1.

A. Neighboring Image Selection

Choosing neighboring images for each reference image is an important part of the whole pipeline. Source images that are close to the reference image may have more overlapping regions, and using them can increase the completeness of the reconstructed result, but it may introduce more errors as large depth change can only cause slight pixel position displacement

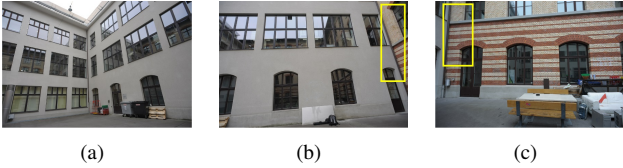


Fig. 2. (b) is the reference image and the rest are source images. Obviously, (a) have more overlapping regions with (b) while the method used by Xu may ignore it and choose (c), as there are more reconstructed sparse 3D points on the yellow regions.

on source images. Source images that are far from the reference image may improve the reconstruction’s accuracy, but they may have fewer overlapping regions and more occlusions, which may decrease the result’s completeness. [24] selects neighboring images using the length of baseline and the angle between principal axes of cameras. It computes the angle ϑ_{ij} between principal axes and the baseline length b_{ij} between the reference image i and the source image j , and filters source images whose $5^\circ \leq \vartheta_{ij} \leq 60^\circ$ and $0.05\bar{b} \leq b_{ij} \leq 2\bar{b}$, \bar{b} is the median baseline length of the reference image i and all of other source images. It sorts source images by $\vartheta_{ij}b_{ij}$ from small to large. However, its super parameters are hard to determine when the scale of scenes and the number of total images varies. The parameter used in [24] even could not work for some scenes in [39]. The strategy used in [26] first filters source images using τ . τ is the projection point’s position displacement when given 3D points a disturb. Its implementation is shown as Eq. 1 and Eq. 2.

$$\hat{\mathbf{X}} = (1 + \epsilon)\mathbf{X} - \epsilon C_i \quad (1)$$

$$\tau = \frac{1}{|A|} \sum_{\mathbf{X} \in A} \|\hat{\mathbf{x}}'_j - \mathbf{x}'_j\| \quad (2)$$

\mathbf{X} represents the back-projected 3D point of \mathbf{x} . First, it gives \mathbf{X} a disturb as Eq. 1, C_i is the camera center of reference image i . It computes the average projection position displacements for points in A as Eq. 2. \mathbf{x}'_j is the 2D coordinate when projecting \mathbf{X} to source image j . $\hat{\mathbf{x}}'_j$ is the 2D coordinate corresponding to $\hat{\mathbf{X}}$. The points in set A are the visible 3D points on both the reference image i and the source image j , and these sparse 3D points are output by SFM software. The method filters source images whose τ is lower than t_τ and sorts the preserved source images with the number of points in A . Then it selects the top 8 images as neighboring images. However, this neighboring image selection method may filter some suitable source images because of the lack of reconstructed points on texture-less regions and stochastic texture regions, as Fig 2 shows. To overcome these weaknesses, we combine these two methods and form our method as shown in equation Eq.3.

$$\zeta = \frac{1}{N_A} \min(b_{ij}, 0.1) \min(\vartheta_{ij}, 0.05) \quad (3)$$

N_A is the number of 3D points in A . We remove the source images whose τ are lower than t_τ to filter source images that are too close to the reference image, and then sort the source images by the value of ζ from small to large, then choose

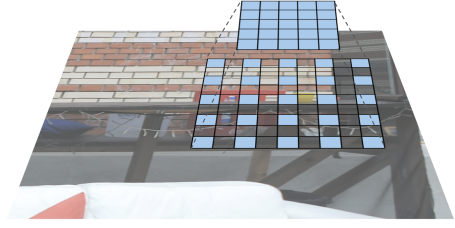


Fig. 3. Schematic diagram of acceleration strategy. As the resize parameters are not necessarily integers, new pixel values will be obtained by interpolation.

the smallest eight source images. Truncation equations are used here to avoid ignoring other parameters of source images whose ϑ or b is too small.

B. Random Initialization

Good initialization can speed up the convergence of the algorithm. Therefore, we adopt the similar method as [26] to random initialize d_x using 2D feature points. It is worth noting that we only consider feature points that correspond to reconstructed sparsely 3D points produced by the SFM software. We choose the closest four feature points in four areas for each pixel, then record the minimum depth value d_{min} and maximum depth value d_{max} among four points. Then we assign a random d_x within $[d_{min}, d_{max}]$ for pixel \mathbf{x} . However, there may be wrong reconstructed 3D points output by the SFM software. Using wrong reconstructed points to initialize the depth may cause the result to be stuck into local optimal and cause errors. So we only consider the 3D points: (1) whose total re-project error is below 2; (2) visible to no smaller than $\lfloor v - 1 \rfloor$ images, where v is the average visible image number of all reconstructed 3D points in one scene; (3) the distance between its corresponding feature point to \mathbf{x} is smaller than $w_r/10$, while w_r is the width of the reference image. To initialize the normal vector for each pixel, we adopt a similar initializing method as [24]. We choose $\theta, \theta \in [0, 2\pi]$ and $\phi, \phi \in [-\pi/2, \pi/2]$ for each pixel and obtain the \mathbf{n}_x as $(\cos\theta \sin\phi, \sin\theta \sin\phi, \cos\phi)$.

C. Depth Map Estimation

Accessing memory on the GPU is time-consuming. Sometimes, we want the matching window size larger when performing stereo matching, as using larger matching windows can make the algorithm more robust. Downsample the image is an intuitive method. However, this strategy may change the value of original pixels and may alter the structure of the original image. As we know, pixel-level differences greatly impact the reconstruction results, especially when the requirement of the result’s accuracy is high. In the experiment section, we show that downsample image is not a good choice as both the accuracy and completeness drop sharply. In order to speed up the algorithm, we borrow the idea from dilated convolution. For simplicity, we call half of the edge length of the square “window radius.” We compute the scale $s = r_{orig}/r_{now}$, r_{orig} is the original matching window radius and r_{now} is the downsampled matching window radius. We compute the

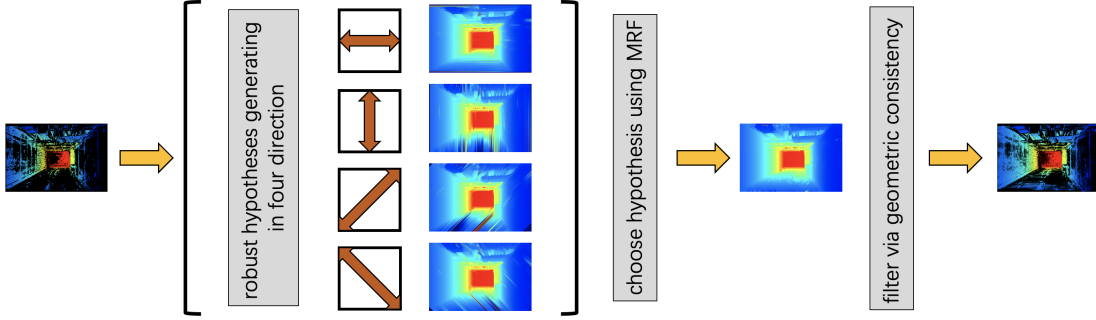


Fig. 4. The pipeline of the plane hypothesis inference procedure. First, we generate four hypotheses using the filtered depth map in four directions. Then the matching cost with each hypothesis is computed. After that, the final hypothesis is selected using MRF. Last, Geometric consistency is considered to filter outliers.

ZNCC values $Z(x, j)$ for each pixel with neighboring image j as shown in Eq.4 and Fig.3. Experiments show that our scheme is effective, and it only slightly influences the result.

$$Z(x, j) = \frac{\sum_{\eta \in W_{now}} (I(\eta) - \bar{I})(I(\eta'_j) - \bar{I}')}{\sqrt{\sum_{\eta \in W_{now}} (I(\eta) - \bar{I})^2} \sqrt{\sum_{\eta \in W_{now}} (I(\eta'_j) - \bar{I}')^2}} \quad (4)$$

$\mathbf{x}(x_1, x_2)$ is the 2D coordinate on images. W_{now} means new coordinates $\eta(\eta_1, \eta_2)$ in the matching window as $\eta_1 \in [x_1 - sr_{now}, x_1 - s(r_{now} - 1), \dots, x_1 + sr_{now}]$, $\eta_2 \in [x_2 - sr_{now}, x_2 - s(r_{now} - 1), \dots, x_2 + sr_{now}]$. η'_j represents the 2D coordinate on neighboring image j which can be obtained by transforming η using the homography mapping. $I(\eta)$ represents the brightness value of η . While η and η'_j may not be integer coordinates, the $I(\eta)$ and $I(\eta'_j)$ will be obtained by computing the bilinear interpolation. \bar{I} and \bar{I}'_j are the average brightness values of $I(\eta)$ and $I(\eta'_j)$ where $\mathbf{x} \in W_{now}$.

$$C(\mathbf{x}) = \frac{\sum_{j \in N} (1 - \delta(C(\mathbf{x}, j), C_{max}))}{\omega \sum_{j \in N} (1 - \delta(C(\mathbf{x}, j), C_{max})) C(\mathbf{x}, j)^{-1}} \quad (5)$$

We use $C(\mathbf{x})$ to represent the integrated matching cost for pixel \mathbf{x} and $C(\mathbf{x}, j) = 1 - Z(\mathbf{x}, j)$ is the matching cost computed using neighboring image j . We give restrictions on calculations. If any η'_j is beyond the border of neighboring image j , we set $C(\mathbf{x}, j)$ to the maximum value $C_{max} = 1 - Z_{min}$. $\delta(a, b) = 1$ if $a = b$ and $\delta(a, b) = 0$ otherwise. Using this strategy, we can reduce the errors caused by distortion, as the distortion of the edge regions of the image will be more serious. We use the similar strategy as [27] to assign each $C(\mathbf{x}, j)$ a weight and the weight is $(C(\mathbf{x}, j))^{-1}$. In summary, the final cost function is as shown in Eq.5. N is the number of neighboring images.

We add random disturbs to the reconstructed result of each pixel after each spatial spreading step to help (d_x, \mathbf{n}_x) jumping out of the local optimal. We random choose $\Delta_d \in [-d_{max}/4, d_{max}/4]$, $\Delta_\theta \in [-\pi/2, \pi/2]$ and $\Delta_\phi \in [-\pi/12, \pi/12]$ and update the d_{old} and \mathbf{n}_{old} to d_{new} and \mathbf{n}_{new} . We use 4 candidates, $(d_{old}, \mathbf{n}_{old})$, $(d_{new}, \mathbf{n}_{old})$,

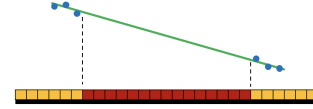


Fig. 5. Orange pixels contain reconstructed depth value and red pixels not. Red pixels will be pad using the green line.

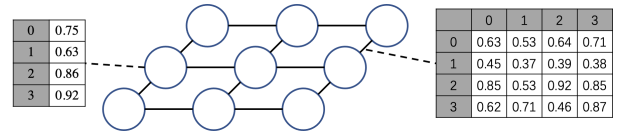


Fig. 6. This is the visualization of our undirected graph model, each node represents for each pixel, each pixel is connected with its four direct neighbors

$(d_{old}, \mathbf{n}_{new})$, $(d_{new}, \mathbf{n}_{new})$. We update the d or \mathbf{n} if the new candidate can generate lower matching cost value. We have also tried more candidates but it can only bring slight improvement with computing time consuming.

D. Depth Map Filtering

We use the geometric consistency to filter outliers. We adopt the similar strategy as that in [40]. \mathbf{x}'_j is the 2D coordinate on image j corresponding to \mathbf{x} that can be obtained using d_x . $d_{\mathbf{x}'_j}$ is obtained by computing bilinear interpolation and $\mathbf{n}_{\mathbf{x}'_j}$ is the same value as $\mathbf{n}_{[\mathbf{x}'_j]}$, $[\mathbf{x}'_j]$ means the rounded coordinate of \mathbf{x}'_j . If the absolute difference between d_x and $d_{\mathbf{x}'_j}$ is smaller than 0.02, the angle between \mathbf{n}_x and $\mathbf{n}_{\mathbf{x}'_j}$ is smaller than 30° and the re-project error is smaller than 1 pixel, we say (d_x, \mathbf{n}_x) is consistent with $(d_{\mathbf{x}'_j}, \mathbf{n}_{\mathbf{x}'_j})$. If (d_x, \mathbf{n}_x) is consistent with more than one $(d_{\mathbf{x}'_j}, \mathbf{n}_{\mathbf{x}'_j})$ among all source images, we reserve (d_x, \mathbf{n}_x) , otherwise, we discard them.

E. Plane Hypothesis Inference

It is hard to use PatchMatch based estimation methods to recover correct depth and normal vectors on texture-less plane regions. Instead of handling this issue by modifying the stereo matching step, we add a module to generate depth hypotheses on pixels that have not been reconstructed correctly. The Plane Hypothesis Inference (PHI) module mainly contains two steps: First, we generate hypotheses for each pixel; Second, we

choose one hypothesis for each empty pixel as new depth. The pipeline of PHI is as shown in Fig.4

To fast generate depth hypotheses, we break down the original depth map into 1D depth arrays with plenty of "holes." "Holes" mean pixels without reconstructed results. We fill "holes" using straight lines, the straight lines are fitted using the closest six neighboring pixels that contain reconstructed depths. We use more than two points to fit the line in order to reduce the impact of noise. As one fitted line can pad a large region of holes as Fig.5 shows, our hypothesis-generating method is efficient. We generate four hypotheses for each non-reconstructed pixel in four directions: horizontal, vertical, 45 degrees below and 45 degrees above. It is shown in Fig.4.

$$\phi_n(h(k, \mathbf{x})) = (C_{max} - C(\mathbf{x}, h(k, \mathbf{x}))) / \kappa_1 + \kappa_2 \quad (6)$$

As the accuracy of the similarity measurement methods such as ZNCC will deteriorate rapidly on texture-less regions, the MRF-based method is more suitable to be used to decide which hypothesis should be chosen. We map Markov Random Field to pairwise Undirected Graph Model(UGM) as Fig.6. Each node represents a pixel on the image. For nodes, $h(k, \mathbf{x})$ is the $k, k \in \{1, 2, 3, 4\}$ depth hypothesis value of \mathbf{x} , $\phi_n(h(k, \mathbf{x}))$ means the value of potential function when choosing $h(k, \mathbf{x})$ and it is shown as Eq.6. κ_1 and κ_2 are used here to weaken the impact of the matching cost. It worth noting that the $C(\mathbf{x}, h(k, \mathbf{x}))$ represent the matching cost computed using $h(k, \mathbf{x})$. Corresponding pixels on neighboring images are obtained by projecting the back-projected 3D point to neighboring images, rather than using homography mapping.

$$\phi_e(h_1, h_2) = \begin{cases} [\kappa_3 - \min(1, (h_1 - h_2)/h_2)]^2, & h_1 > h_2 \\ [\kappa_3 - \min(1, (h_2 - h_1)/h_1)]^2, & else \end{cases} \quad (7)$$

For edges, the potential function $\phi_e(h(k_1, \mathbf{x}_1), h(k_2, \mathbf{x}_2))$ is computed using the relative difference between hypothesis values of two connected nodes as Eq.7. For brevity, we note it as $p_e(h_1, h_2)$. Truncation functions are used here to avoid depth values which near to the edge part over-smoothed.

$$\mathbf{P} = \frac{1}{Z} \prod_n \phi_n(h(k, \mathbf{x})) \prod_e \phi_e(h_1, h_2) \quad (8)$$

$$Z = \sum_k \overbrace{\cdots}^{\text{pixel number}} \sum_k \prod_n \phi_n(h(k, \mathbf{x})) \prod_e \phi_e(h_1, h_2) \quad (9)$$

In pairwise UGM, the state of each node is only related to its connected nodes. The joint probability \mathbf{P} is shown as Eq.8. Normalization constant Z is simply the scalar value that forces the distribution to sum to one. In general cases, the decoding procedure of UGM is an NP-hard problem, we use the approximate technique TRW to perform the decoding. In order to speed up the decoding process and reduce memory usage. We first downsample the hypothesis map to half of its original size, decoding UGM, and then obtaining the downsampled padded hypothesis map. Then we up-sample the

padded hypothesis map and regard it as the depth reference map. Last, we choose the closest hypothesis to the hypothesis reference map for each pixel.

$$n = \frac{(\mathbf{X}_u - \mathbf{X}_d) \times (\mathbf{X}_l - \mathbf{X}_r)}{\|(\mathbf{X}_u - \mathbf{X}_d) \times (\mathbf{X}_l - \mathbf{X}_r)\|^2} \quad (10)$$

The normal vectors of padded pixels do not exist, and we adopt the similar normal vectors computing method as [27]. The normal vectors of these regions are computed using the four neighboring pixels of each pixel as shown in Eq.10. $\mathbf{X}_u, \mathbf{X}_d, \mathbf{X}_l, \mathbf{X}_r$ are the back projected 3D points of 4-connected neighboring pixels of \mathbf{x} . After that, we again use geometric consistency to filter outliers. PHI is carried out on consumer-grade CPUs and can significantly improve the result with acceptable time consumption.

F. Depth Map Fusion

We back project each pixel on reference image i to 3D space and obtain \mathbf{X}_i , then back project the corresponding pixels whose coordinate are $[\mathbf{x}'_j]$ on all other images and obtain \mathbf{X}'_j . If the relative difference between \mathbf{X}_i and \mathbf{X}'_j is smaller than 0.01, we delete the corresponding pixel on image j and merge \mathbf{X}_i and \mathbf{X}'_j by taking the average of them. After handling all pixels on image i , we delete image i . And then, we perform the same operation on the remaining images.

IV. EXPERIMENTAL RESULTS AND DISCUSSION

In order to show the effectiveness of our method, we have tested it on ETH3D high-resolution benchmark[39], whose image resolution is 6048×4032 . ETH3D provides the calibration results and SFM sparse reconstruction. It uses F1 score, completeness and accuracy to measure the quality of results. ETH3D contains 13 scenes for training and 12 scenes for testing. In order to make our algorithm running within an acceptable time, we resize images to half of their original size while keeping the original aspect ratio. PHI-MVS is implemented using C++ with CUDA, Eigen, PCL and OpenCV. For decoding UGM, we use the open-sourced library DGM[42]. Our algorithm is executed on a computer equipped with an Intel Core i5 9400F CPU and an NVIDIA RTX 3070 GPU. In our experiment, we verify the effectiveness of two main improvements separately. As the test set results can be upload only once a week, we only use the training set to perform the ablation study. The parameter $\{r_{now}, r_{orig}, \kappa_1, \kappa_2, \kappa_3, \epsilon, t_\tau\}$ we used are $\{5, 7, 4, 0.5, 2, 0.002, 0.1\}$. The total iteration number of spatial spreading is eight. The decoding procedure of UGM is only iterated once.

A. Plane Hypothesis Inference

Our Plane Hypothesis Inference strategy can significantly improve the reconstruction of texture-less regions. Without our padding module, most of the texture-less regions could not be correctly estimated as ZNCC could not correctly measure the similarity on these regions. As shown in Fig.7, our strategy is effective, especially on some indoor scenes, which contain plenty of man-made texture planes. In order to



Fig. 7. The first columns are input images; the second columns are the point cloud results of PHI-MVS/P; the third columns are point cloud results of our whole pipeline. These results are reconstructed from delivery area, kicker and terrace from ETH high-resolution training set.

TABLE I
EVALUATION RESULTS ON THE HIGH-RESOLUTION MULTI-VIEW TRAINING DATASETS OF ETH3D BENCHMARK. F1 SCORES ARE EVALUATED AT DIFFERENT TOLERANCE (1CM, 2CM, 5CM AND 10 CM).

Data Set	PHI-MVS/P				PHI-MVS/M				PHI-MVS			
	1cm	2cm	5cm	10cm	1cm	2cm	5cm	10cm	1cm	2cm	5cm	10cm
courty.	65.19	85.06	93.92	96.86	66.45	86.12	94.78	97.49	66.83	86.40	94.96	97.60
delive.	70.09	85.00	94.18	97.20	73.93	89.09	96.99	98.66	74.83	89.52	97.06	98.65
electro	68.47	80.78	90.24	94.90	73.16	85.20	93.06	96.48	73.88	85.52	93.11	96.49
facade	48.25	68.66	86.82	92.46	48.86	69.23	87.65	93.08	49.32	69.53	87.71	93.13
kicker	57.97	68.63	81.33	89.83	68.68	81.74	90.81	94.26	70.61	82.38	90.71	94.07
meadow	39.28	55.46	70.11	78.26	49.45	64.34	79.67	87.16	50.93	65.67	80.78	87.91
office	49.99	61.80	75.94	85.33	67.50	80.25	92.17	96.91	69.62	81.35	92.40	97.12
pipes	59.50	68.67	82.03	91.23	73.50	81.38	90.31	96.72	74.84	82.36	91.03	97.17
playgr.	54.96	71.34	87.08	93.53	56.75	72.72	87.62	93.92	57.25	73.07	87.68	93.90
relief.	73.35	84.25	91.88	95.44	75.17	86.93	94.20	96.54	75.53	87.31	94.32	96.46
relief.	71.62	83.68	92.26	95.87	73.87	86.39	94.34	96.96	74.32	86.76	94.48	96.93
terrace	75.37	86.88	94.76	98.08	77.84	89.06	96.23	98.65	78.35	89.24	96.21	98.64
terrai.	75.32	84.28	92.00	96.08	83.06	91.00	96.03	98.07	84.17	91.56	96.16	98.10
average	62.26	75.73	87.12	92.70	68.32	81.80	91.84	95.76	69.27	82.36	92.05	95.86

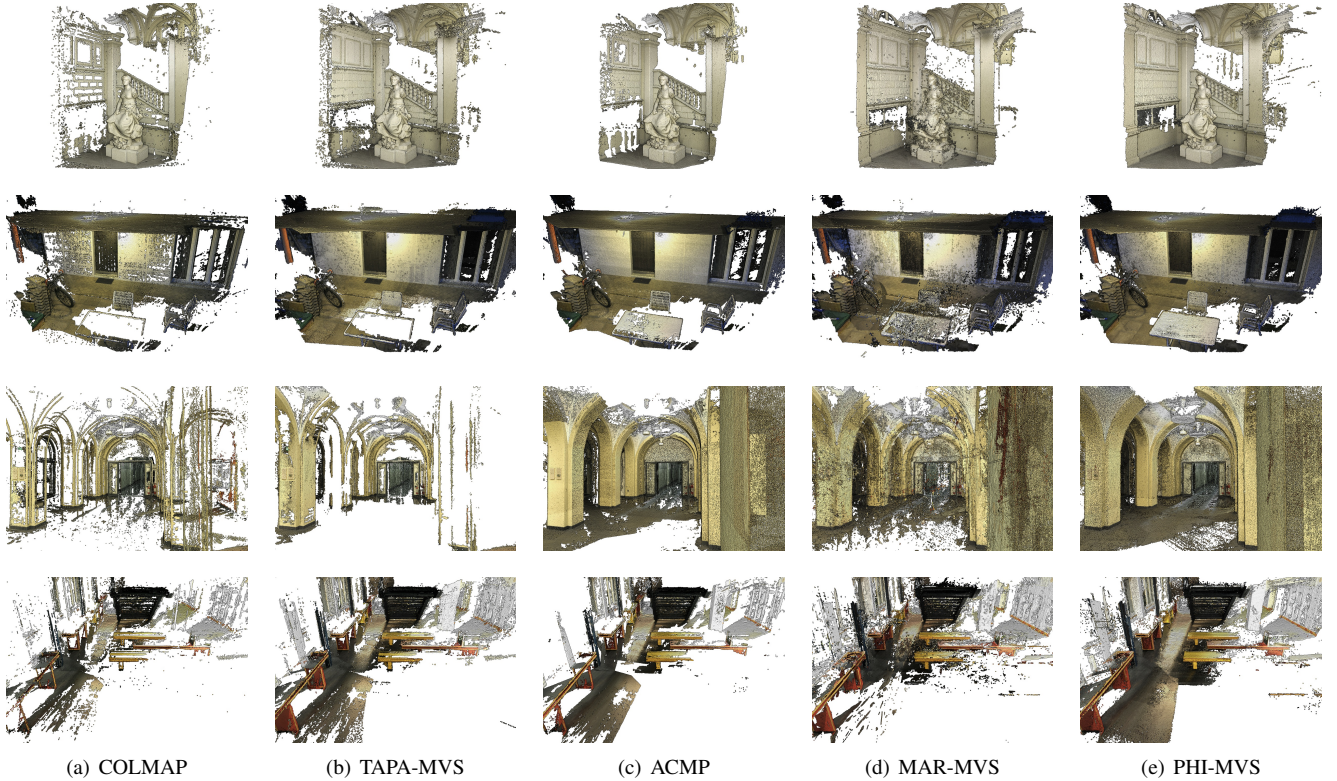


Fig. 8. Comparison to state-of-the-art algorithms on some data sets (statue, terrace, old computer and lecture) of ETH3D benchmark. These point cloud models are shown by the ETH3D evaluation server.

TABLE II

EVALUATION RESULTS ON THE HIGH-RESOLUTION MULTI-VIEW TEST DATASETS OF ETH3D BENCHMARK. F1 SCORE, ACCURACY, AND COMPLETENESS AT DIFFERENT TOLERANCE (1CM, 2CM AND 5CM).

Method	1cm			2cm			5cm			10cm		
	F1	A	C	F1	A	C	F1	A	C	F1	A	C
PHI-MVS	75.8	74.92	77.49	86.43	86.38	86.83	93.89	94.34	93.59	96.77	96.96	96.65
MAR-MVS[26]	71.51	67.72	76.76	81.84	80.24	84.18	90.30	90.32	90.63	94.22	94.21	94.43
MGMVS[33]	73.96	70.47	78.42	83.41	80.32	87.11	91.77	89.54	94.25	95.61	94.08	97.24
CLD-MVS[27]	73.33	72.88	75.60	82.31	83.18	82.73	89.47	91.82	87.97	92.98	95.47	91.06
ACMP[28]	72.30	82.64	66.24	81.51	90.54	75.58	89.01	95.71	84.00	92.62	97.47	88.71
ACMM[38]	70.80	82.11	64.35	80.78	90.65	74.34	89.14	96.30	83.72	92.96	98.05	88.77
PCF-MVS[41]	70.95	72.70	70.10	80.38	82.15	79.29	87.74	89.12	86.77	91.56	92.12	91.26
TAPA-MVS[37]	66.60	75.16	61.82	79.15	85.71	74.94	88.16	92.49	85.02	92.30	94.93	90.35
COLMAP[40]	61.27	83.75	50.90	73.01	91.97	62.98	83.96	96.75	75.74	90.40	98.25	84.54

the effectiveness of the whole PHI module, we remove the PHI module and note it as PHI-MVS/P. As we use MRF to perform the plane hypothesis selecting process, we show its effectiveness by removing the MRF, and select the hypothesis with the minimal matching cost for each pixel. We note the pipeline without MRF as PHI-MVS/M. We test the above three pipelines on the ETH training sets, which contain 13 scenes. As shown in Tab.I By using PHI module, the reconstructed result can be significantly improved. Using MRF to choose hypotheses can make the result achieve a higher F1 score in low tolerance of each scene. It can make the algorithm more robust as PHI-MVS achieves the highest average F1 score under each tolerance. The total running time of the additional

module is about 9s, and the most time-consuming part is the graph building step which could not be executed in parallel. The decoding procedure using TRW only costs about 2-3 seconds on the consumer-grade CPUs. The F1 score, running time all show that PHI module is efficient and effective.

B. Speed up scheme

We increase the matching window radius from 5 to 10, correspondingly, the window side length increases from 11 to 21. We run our whole pipeline with different r_{now} and r_{orig} , the results of F1 scores under different tolerance and running times of depth map estimation step are shown in the TabIII. It can be seen that by using our speed-up scheme, the depth

Algorithm 1 PHI-MVS pipeline**Input:** images and SFM sparse reconstruction result**Output:** merged point cloud

```

1: /*neighboring images selection*/
2: for each reference image do
3:   sort images as Eq.3, choose top 8 as neighboring images
4: end for
5: /*random initialization*/
6: for each reference image do
7:   for each pixel do
8:     initialize depth with 4 points or random value
9:     initialize normal vectors with random values
10:  end for
11: end for
12: /*depth map estimation*/
13: for each reference image do
14:   while iteration  $\leq$  total iteration number do
15:     red and black checkerboard updating
16:     random refinement
17:   end while
18: end for
19: /*depth map filtering*/
20: for each reference image do
21:   filter outliers with geometric consistency
22: end for
23: /*plane hypothesis inference*/
24: for each reference image do
25:   load filtered depth map
26:   generate depth hypotheses
27:   compute matching cost with generated hypotheses
28:   downsample hypotheses maps
29:   build and decode UGM
30:   select hypothesis using decoding result
31: end for
32: /*depth map filtering*/
33: for each reference image do
34:   filter outliers with geometric consistency
35: end for
36: fusion
37: /*fusion*/
38: for each reference image do
39:   back project pixels and merge points
40: end for

```

map estimation step can be executed faster, especially when r_{orig} is large. The result is only slightly changed comparing with that computed using the original matching window size. We also downsample images to a quarter of their original size. Though this strategy can save computing time, the F1 score drops sharply. The F1 score drops 11.67, 6.02, 3.06, 2.00 under tolerance 1cm, 2cm, 5cm, 10cm. It can be seen that our scheme is a good choice to balance the speed and the performance.

C. Overall Evaluation

The evaluation of our algorithm's whole pipeline is performed on the test set of the ETH3D high-resolution multi-view dataset. Our result has achieved state-of-the-art results

TABLE III

EVALUATION RESULTS ON THE HIGH-RESOLUTION MULTI-VIEW TRAINING DATASETS OF ETH3D BENCHMARK. F1 SCORE AND RUNNING TIMES ARE EVALUATED AT DIFFERENT TOLERANCE (1CM, 2CM, 5CM AND 10CM). METHODS MEANS THE ALGORITHM WITH DIFFERENT MATCHING WINDOW RADIUS. THE FIRST NUMBER IS r_{now} AND THE SECOND IS r_{orig} .

Method	F1 Score				Time(s)
	1cm	2cm	5cm	10cm	
5/5	69.17	82.28	91.80	95.63	9.79
5/6	69.34	82.40	91.98	95.81	10.02
6/6	69.23	82.38	91.99	95.83	12.58
5/7	69.27	82.36	92.05	95.86	9.57
7/7	69.11	82.29	92.05	95.95	16.41
5/8	69.04	82.16	91.98	95.88	10.04
8/8	68.69	81.97	91.92	95.90	20.92
5/9	68.70	81.85	91.85	95.83	10.51
9/9	68.23	81.58	91.73	95.83	25.91
5/10	68.38	81.62	91.70	95.78	10.86
10/10	67.89	81.27	91.50	95.73	31.60

among the published algorithms. Besides, our algorithm is efficient and can be executed within an acceptable time. The comparison with other algorithms is shown in Fig.8 and TableII. It can be seen that our new pipeline can obtain a better trade-off between accuracy and completeness.

V. CONCLUSION

In this paper, we present a novel MVS pipeline which is called Plane Hypothesis Inference Multi-View Stereo(PHI-MVS). The additional PHI module can significantly improve the reconstruction of texture-less regions in two steps. First, it generates multiple plane hypotheses from initial depth maps using a robust padding strategy, and then chooses depth hypotheses for each pixel using Markov Random Field. Besides, a speed-up scheme similar to dilated convolution is used to speed up our algorithm. Experimental results on the ETH3D benchmark show that PHI-MVS is efficient and effective. In future works, we plan to improve the accuracy of the reconstructed results using local texture information.

REFERENCES

- [1] C. Wu, "Towards linear-time incremental structure from motion," in *2013 International Conference on 3D Vision-3DV 2013*. IEEE, 2013, pp. 127–134.
- [2] J. L. Schonberger and J.-M. Frahm, "Structure-from-motion revisited," in *Proceedings of the IEEE conference on computer vision and pattern recognition*, 2016, pp. 4104–4113.
- [3] A. J. Davison, I. D. Reid, N. D. Molton, and O. Stasse, "Monoslam: real-time single camera slam," *IEEE Transactions on Pattern Analysis and Machine Intelligence*, vol. 29, no. 6, pp. 1052–1067, 2007.
- [4] R. A. Newcombe, S. J. Lovegrove, and A. J. Davison, "Dtam: Dense tracking and mapping in real-time," in *IEEE International Conference on Computer Vision, ICCV 2011, Barcelona, Spain, November 6-13, 2011*, 2011.
- [5] L. Maier-Hein, P. Mountney, A. Bartoli, H. Elhawary, D. Elson, A. Groch, A. Kolb, M. Rodrigues, J. Sorger, and S. Speidel, "Optical techniques for 3d surface reconstruction in computer-assisted laparoscopic surgery," *Medical Image Analysis*, vol. 17, no. 8, pp. 974–996, 2013.
- [6] M. Park, J. Luo, A. C. Gallagher, and M. Rabbani, "Learning to produce 3d media from a captured 2d video," *IEEE transactions on multimedia*, vol. 15, no. 7, pp. 1569–1578, 2013.

- [7] C. Barnes, E. Shechtman, A. Finkelstein, and D. B. Goldman, "Patchmatch: A randomized correspondence algorithm for structural image editing," *ACM Trans. Graph.*, vol. 28, no. 3, p. 24, 2009.
- [8] F. Yu and V. Koltun, "Multi-scale context aggregation by dilated convolutions," *arXiv preprint arXiv:1511.07122*, 2015.
- [9] S. M. Seitz, B. Curless, J. Diebel, D. Scharstein, and R. Szeliski, "A comparison and evaluation of multi-view stereo reconstruction algorithms," in *2006 IEEE computer society conference on computer vision and pattern recognition (CVPR'06)*, vol. 1. IEEE, 2006, pp. 519–528.
- [10] M. Goesele, B. Curless, and S. M. Seitz, "Multi-view stereo revisited," in *IEEE Computer Society Conference on Computer Vision & Pattern Recognition*, 2006.
- [11] I. Kostrikov, E. Horbert, and B. Leibe, "Probabilistic labeling cost for high-accuracy multi-view reconstruction," in *Computer Vision & Pattern Recognition*, 2014.
- [12] C. H. Esteban and F. Schmitt, "Silhouette and stereo fusion for 3d object modeling," in *Fourth International Conference on 3-D Digital Imaging and Modeling, 2003. 3DIM 2003. Proceedings.*, 2003.
- [13] Y. Furukawa and J. Ponce, "Accurate, dense, and robust multiview stereopsis," *Pattern Analysis and Machine Intelligence, IEEE Transactions on*, vol. 32, no. 8, pp. p.1362–1376, 2010.
- [14] Engin, Tola, Christoph, Strecha, Pascal, and Fua, "Efficient large-scale multi-view stereo for ultra high-resolution image sets," *Machine Vision and Applications*, vol. 23, no. 5, pp. 903–920, 2011.
- [15] M. Goesele, N. Snavely, B. Curless, H. Hoppe, and S. M. Seitz, "Multi-view stereo for community photo collections," in *Computer Vision, 2007. ICCV 2007. IEEE 11th International Conference on*, 2007.
- [16] P. Wu, Y. Liu, Y. Mao, L. Jie, and S. Du, "Fast and adaptive 3d reconstruction with extensively high completeness," *IEEE Transactions on Multimedia*, vol. 19, no. 2, pp. 266–278, 2017.
- [17] Y. Boykov, O. Veksler, and R. Zabih, "Fast approximate energy minimization via graph cuts," in *Proceedings of the Seventh IEEE International Conference on Computer Vision*, 1999.
- [18] Y. Boykov and V. Kolmogorov, "An experimental comparison of min-cut/max-flow algorithms for energy minimization in vision," *IEEE Transactions on Pattern Analysis and Machine Intelligence*, vol. 26, no. 9, pp. 1124–1137, 2004.
- [19] V. Kolmogorov, "Convergent tree-reweighted message passing for energy minimization," *IEEE transactions on pattern analysis and machine intelligence*, vol. 28, no. 10, pp. 1568–1583, 2006.
- [20] N. D. Campbell, G. Vogiatzis, C. Hernández, and R. Cipolla, "Using multiple hypotheses to improve depth-maps for multi-view stereo," in *European Conference on Computer Vision*. Springer, 2008, pp. 766–779.
- [21] V. Kolmogorov and R. Zabih, "What energy functions can be minimized via graph cuts?" *IEEE Trans Pattern Anal Mach Intell*, vol. 26, no. 2, pp. 147–159, 2004.
- [22] J. S. Yedidia, W. T. Freeman, and Y. Weiss, "Generalized belief propagation," *Advances in Neural Information Processing Systems 13, Papers from Neural Information Processing Systems (NIPS) 2000, Denver, CO, USA*, 2001.
- [23] M. Bleyer, C. Rhemann, and C. Rother, "Patchmatch stereo-stereo matching with slanted support windows," in *Bmvc*, vol. 11, 2011, pp. 1–11.
- [24] S. Shen, "Accurate multiple view 3d reconstruction using patch-based stereo for large-scale scenes," *IEEE transactions on image processing*, vol. 22, no. 5, pp. 1901–1914, 2013.
- [25] S. Galliani, K. Lasinger, and K. Schindler, "Massively parallel multiview stereopsis by surface normal diffusion," in *Proceedings of the IEEE International Conference on Computer Vision*, 2015, pp. 873–881.
- [26] Z. Xu, Y. Liu, X. Shi, Y. Wang, and Y. Zheng, "Marmvs: Matching ambiguity reduced multiple view stereo for efficient large scale scene reconstruction," in *Proceedings of the IEEE/CVF Conference on Computer Vision and Pattern Recognition*, 2020, pp. 5981–5990.
- [27] Z. Li, W. Zuo, Z. Wang, and L. Zhang, "Confidence-based large-scale dense multi-view stereo," *IEEE Transactions on Image Processing*, vol. 29, pp. 7176–7191, 2020.
- [28] Q. Xu and W. Tao, "Planar prior assisted patchmatch multi-view stereo," in *AAAI*, 2020, pp. 12 516–12 523.
- [29] Y. Yao, Z. Luo, S. Li, T. Fang, and L. Quan, "Mvsnet: Depth inference for unstructured multi-view stereo," in *Proceedings of the European Conference on Computer Vision (ECCV)*, 2018, pp. 767–783.
- [30] H. Yi, Z. Wei, M. Ding, R. Zhang, Y. Chen, G. Wang, and Y.-W. Tai, "Pyramid multi-view stereo net with self-adaptive view aggregation," in *European Conference on Computer Vision*. Springer, 2020, pp. 766–782.
- [31] Y. Xue, J. Chen, W. Wan, Y. Huang, C. Yu, T. Li, and J. Bao, "Mvsrft: Learning multi-view stereo with conditional random fields," in *Proceedings of the IEEE International Conference on Computer Vision*, 2019, pp. 4312–4321.
- [32] K. Luo, T. Guan, L. Ju, Y. Wang, Z. Chen, and Y. Luo, "Attention-aware multi-view stereo," in *Proceedings of the IEEE/CVF Conference on Computer Vision and Pattern Recognition*, 2020, pp. 1590–1599.
- [33] Y. Wang, T. Guan, Z. Chen, Y. Luo, and L. Ju, "Mesh-guided multi-view stereo with pyramid architecture," in *2020 IEEE/CVF Conference on Computer Vision and Pattern Recognition (CVPR)*, 2020.
- [34] H. Aanæs, R. R. Jensen, G. Vogiatzis, E. Tola, and A. B. Dahl, "Large-scale data for multiple-view stereopsis," *International Journal of Computer Vision*, pp. 1–16, 2016.
- [35] A. Knapitsch, J. Park, Q.-Y. Zhou, and V. Koltun, "Tanks and temples: Benchmarking large-scale scene reconstruction," *ACM Transactions on Graphics*, vol. 36, no. 4, 2017.
- [36] Q. Xu and W. Tao, "Pvsnet: Pixelwise visibility-aware multi-view stereo network," *arXiv preprint arXiv:2007.07714*, 2020.
- [37] A. Romanoni and M. Matteucci, "Tapa-mvs: Textureless-aware patchmatch multi-view stereo," in *Proceedings of the IEEE International Conference on Computer Vision*, 2019, pp. 10413–10422.
- [38] Q. Xu and W. Tao, "Multi-scale geometric consistency guided multi-view stereo," in *Proceedings of the IEEE Conference on Computer Vision and Pattern Recognition*, 2019, pp. 5483–5492.
- [39] T. Schöps, J. L. Schönberger, S. Galliani, T. Sattler, K. Schindler, M. Pollefeys, and A. Geiger, "A multi-view stereo benchmark with high-resolution images and multi-camera videos," in *Conference on Computer Vision and Pattern Recognition (CVPR)*, 2017.
- [40] J. L. Schönberger, E. Zheng, M. Pollefeys, and J.-M. Frahm, "Pixelwise view selection for unstructured multi-view stereo," in *European Conference on Computer Vision (ECCV)*, 2016.
- [41] A. Kuhn, S. Lin, and O. Erdler, "Plane completion and filtering for multi-view stereo reconstruction," in *German Conference on Pattern Recognition*. Springer, 2019, pp. 18–32.
- [42] S. Kosov, "Direct graphical models c++ library," <http://research.project-10.de/dgml>, 2013.